JUSTC

Letter

http://justc.ustc.edu.cn

Received: February 23, 2024; Accepted: April 01, 2024

Charge-balanced codoping enables exceeding doping limit and ultralow thermal conductivity

Long Chen[1], Chun Wang[1], Lin Wang[1], Minghao Wang[2], Yongchun Zhu[1,2] ✉, and Changzheng Wu[1,3] ✉

[1]*School of Chemistry and Materials Science, University of Science and Technology of China, Hefei 230026, China;*
[2]*Hefei National Research Center for Physical Sciences at the Microscale, University of Science and Technology of China, Hefei 230026, China;*
[3]*Institute of Energy, Hefei Comprehensive National Science Center, Hefei 230031, China*

✉Correspondence: Yongchun Zhu, E-mail: ychzhu@ustc.edu.cn; Changzheng Wu, E-mail: czwu@ustc.edu.cn

Graphical abstract

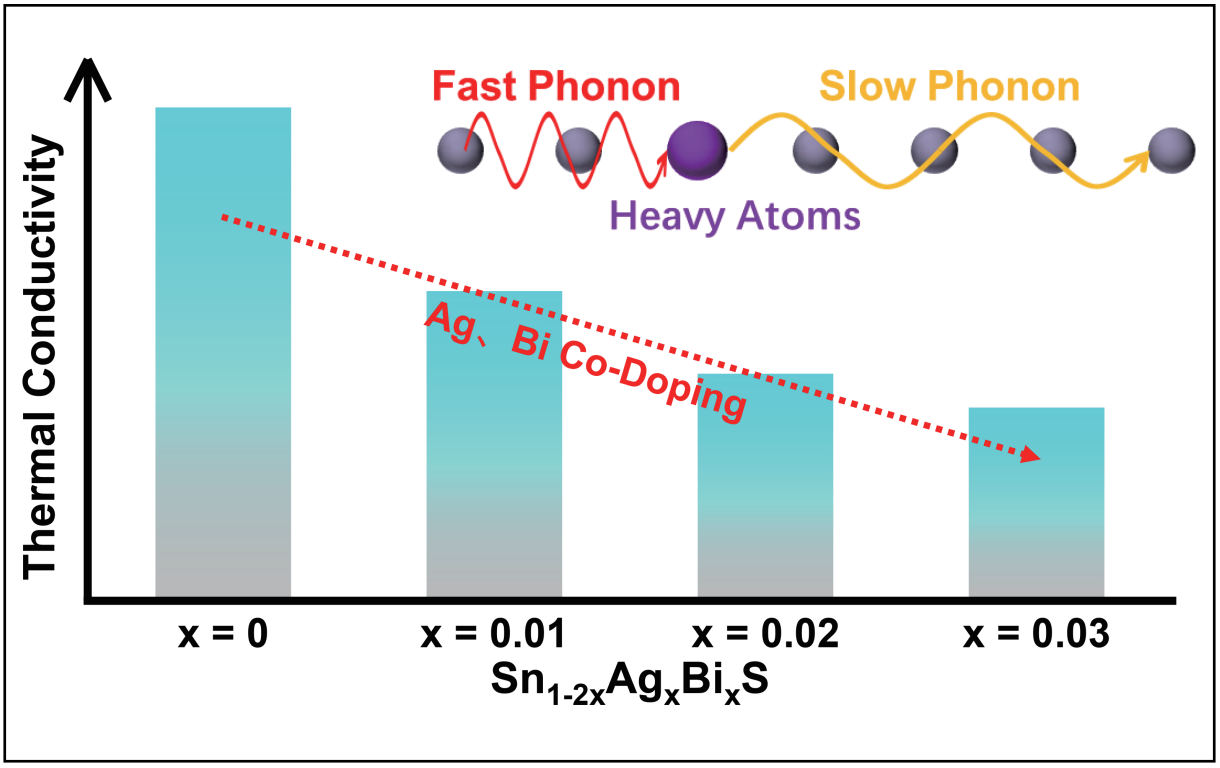

Ag, Bi codoping leads to ultralow thermal conductivity in SnS.

Public summary

- Codoping Bi with Ag increases the solubility of Ag from 2% to 3% because of the charge balance, increasing the scattering center concentration to three times that of SnS doped with Ag alone.
- The lowest thermal conductivity appears for $Ag_{0.03}Bi_{0.03}Sn_{0.94}S$, 0.535 $W \cdot m^{-1} \cdot K^{-1}$ at room temperature and 0.388 $W \cdot m^{-1} \cdot K^{-1}$ at 275 °C, below the amorphous limit of SnS (0.45 $W \cdot m^{-1} \cdot K^{-1}$), which is a tremendous increase.
- Point defects at the atomic scale and grain boundaries at the nanoscale scatter phonons synergistically, providing insight into ultralow thermal conductivity.

Citation: Chen L, Wang C, Wang L, et al. Charge-balanced codoping enables exceeding doping limit and ultralow thermal conductivity. *JUSTC*, **2024**, 54(6): 0601. DOI: 10.52396/JUSTC-2024-0025

JUSTC

Letter

http://justc.ustc.edu.cn

Received: February 23, 2024; Accepted: April 01, 2024

Charge-balanced codoping enables exceeding doping limit and ultralow thermal conductivity

Long Chen[1], Chun Wang[1], Lin Wang[1], Minghao Wang[2], Yongchun Zhu[1,2] ✉, and Changzheng Wu[1,3] ✉

[1]*School of Chemistry and Materials Science, University of Science and Technology of China, Hefei 230026, China;*
[2]*Hefei National Research Center for Physical Sciences at the Microscale, University of Science and Technology of China, Hefei 230026, China;*
[3]*Institute of Energy, Hefei Comprehensive National Science Center, Hefei 230031, China*

✉Correspondence: Yongchun Zhu, E-mail: ychzhu@ustc.edu.cn; Changzheng Wu, E-mail: czwu@ustc.edu.cn

Cite This: *JUSTC*, **2024**, 54(6): 0601 (7pp)

Read Online

SI Supporting Information

Abstract: Materials with low thermal conductivity are applied extensively in energy management, and breaking the amorphous limits of thermal conductivity to solids has attracted widespread attention from scientists. Doping is a common strategy for achieving low thermal conductivity that can offer abundant scattering centers in which heavier dopants always result in lower phonon group velocities and lower thermal conductivities. However, the amount of equivalent heavy-atom single dopant available is limited. Unfortunately, nonequivalent heavy dopants have finite solubility because of charge imbalance. Here, we propose a charge balance strategy for SnS by substituting Sn^{2+} with Ag^{+} and heavy Bi^{3+}, improving the doping limit of Ag from 2% to 3%. Ag and Bi codoping increases the point defect concentration and introduces abundant boundaries simultaneously, scattering the phonons at both the atomic scale and nanoscale. The thermal conductivity of $Ag_{0.03}Bi_{0.03}Sn_{0.94}S$ decreased to 0.535 $W\cdot m^{-1}\cdot K^{-1}$ at room temperature and 0.388 $W\cdot m^{-1}\cdot K^{-1}$ at 275 ℃, which is below the amorphous limit of 0.450 $W\cdot m^{-1}\cdot K^{-1}$ for SnS. This strategy offers a simple way to enhance the doping limit and achieve ultralow thermal conductivity in solids below the amorphous limit without precise structural modification.

Keywords: charge-balanced codoping; heavy atom; point defect; grain boundary; ultralow thermal conductivity

CLC number: TB34 **Document code:** A

1 Introduction

Exploring the thermal insulation limit of materials has been a popular research topic in recent years, and these materials have great application value in fields such as aerospace[1,2], integrated semiconductors[3], and thermoelectric conversion[4,5]. The heat conduction in solid materials mainly comes from phonons (lattice vibrations)[6]. Different crystals usually have different phonon group velocities and relaxation times and thus have different thermal conductivities. Generally, heavier atoms, weaker bonds and more complex structures all contribute to lower thermal conductivity[7]. Therefore, reducing the thermal conductivity of solid materials mainly focuses on the design of the material structure to limit the transmission of phonons in solids. Previous studies have focused on the formation of superlattices[8–10], anisotropic bonding[3,11], and the introduction of defect engineering[12–14], which all decrease the thermal conductivity by enhancing phonon scattering and reducing the mean free path of phonons.

Defect engineering is a simple and effective method that can significantly reduce thermal conductivity[15,16]. Dopants with heavy atomic masses and compatible radii and charges are ideal candidates. After doping, phonons are generally scattered by defects. The heavier the dopant is, the stronger the scattering is[17]. The smaller the "size difference" of the dopant is, the greater the doping concentration, and thus, the more scattering centers there are[18]. When the doping atoms are equivalent to the host atoms, the whole system charge can be balanced, but the available doping elements are limited. Taking dopants for SnS as an example, Ge^{2+} has a lighter mass and smaller radius, and Pb^{2+} is toxic[19]. Nonequivalent atoms used for doping always have limited solubility or instability due to charge imbalance, resulting in the concentration of confined point defects, so the decrease in thermal conductivity is limited[20–24]. Considering the ionic radius, Tl^{+} is more suitable for SnS than Ag^{+}, but Tl^{+} is toxic, so there are more studies on Ag-doped SnS[24]. In Ag-doped SnS, for example, because of charge mismatch, the doping amount of Ag is limited to less than 2%, so it is difficult to increase the thermal conductivity to a much lower level[18,25]. Exceeding the normal doping limit is favorable for more point defects, which may be effective for realizing a further decrease in thermal conductivity.

In this article, we report a charge-balanced codoping strategy for SnS to effectively improve the impurity doping content. Trivalent Bi^{3+} with a heavy atomic mass and an ionic radius similar to that of Sn^{2+} was screened out as a codopant of Ag^{+} in SnS to achieve ultralow thermal conductivity (Fig. 1a). By utilizing equal amounts of trivalent Bi ions and monovalent Ag-codoped SnS, the doping content of Ag increased from 2% to 3%, and the number of impurity atoms increased by three times. At the same time, the atomic mass difference between Bi and Sn is greater than that between Ag

DOI: 10.52396/JUSTC-2024-0025
JUSTC, **2024**, 54(6): 0601

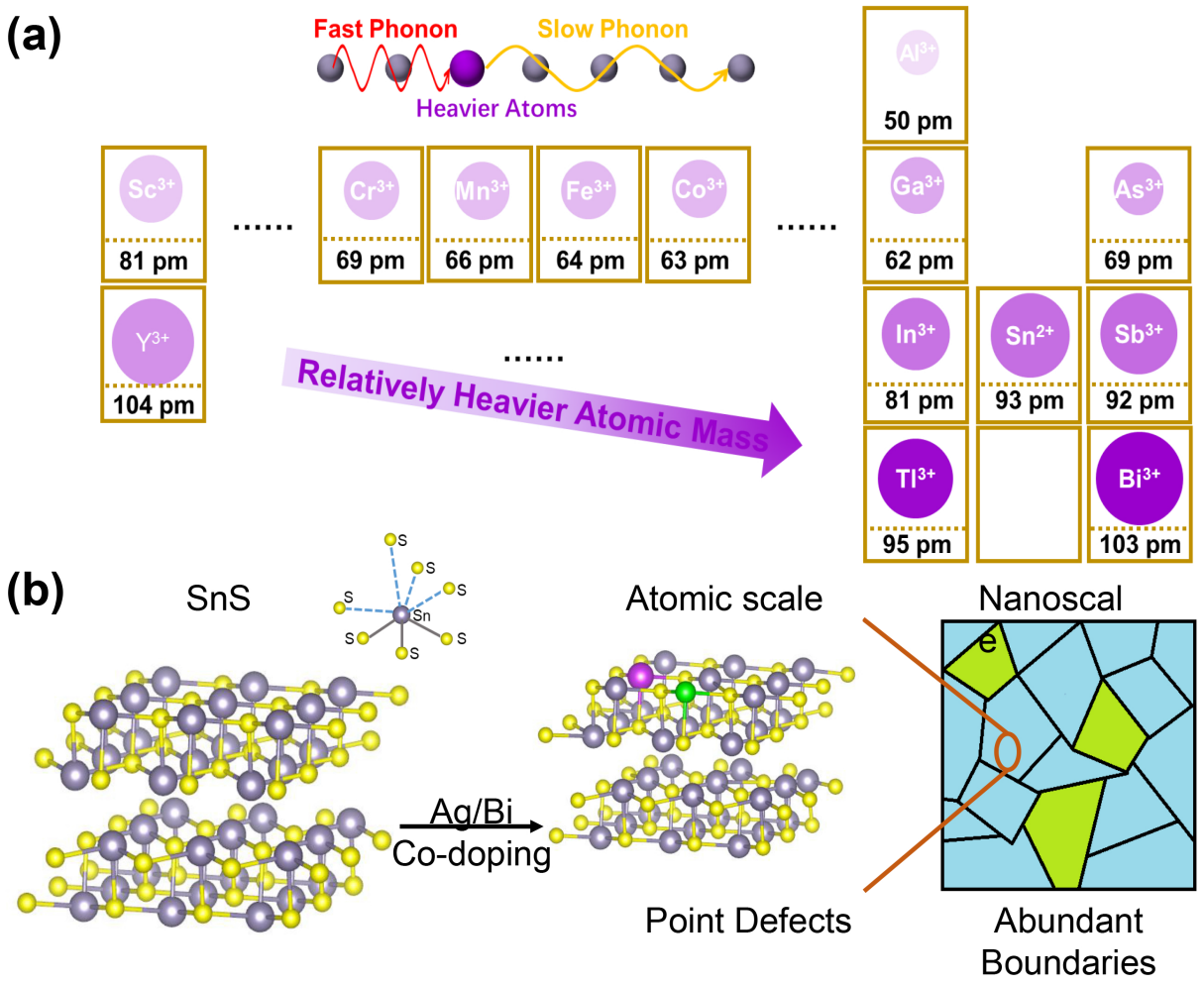

Fig. 1. (a) Illustration of atomic mass of metals with trivalent ions. Darker colors mean heavier atomic mass, and the radii of the circles reflect of their trivalent ions. Top scheme shows phonons' group velocity declines when meeting with heavier atoms. (b) Illustration of SnS crystal structure and changes after charge balance codoping, in which gray, yellow, purple and green balls refers to Sn^{2+}, S^{2-}, Bi^{3+} and Ag^{+}, respectively.

and Sn, strengthening point defect scattering. In addition, the doping of heteroatoms also reduced the grain size of polycrystalline SnS and increased the grain boundary scattering of phonons, as shown in Fig. 1b. Accordingly, the thermal conductivity of $Ag_{0.03}Bi_{0.03}Sn_{0.94}S$ decreased to 0.535 $W \cdot m^{-1} \cdot K^{-1}$ at room temperature, which is two times lower than that of SnS. The thermal conductivity gradually decreased with increasing temperature and reached as low as 0.388 $W \cdot m^{-1} \cdot K^{-1}$ at 275 °C, which is lower than the amorphous limit of SnS[26–29]. This work provides new ways to overcome the low thermal conductivity limit of solid materials by enhancing the doping limit.

2 Experiments

High-purity raw materials of Sn, S, Ag and Bi were weighed and mixed in quartz tubes according to the stoichiometric ratio of $Sn_{1-2x}Ag_xBi_xS$ (x = 0, 0.01, 0.02, 0.03), with the total mass fixed at 4.000 g. The tubes with the raw materials were evacuated and flame-sealed under a pressure of 10^{-3} Pa. The samples were heated to 873 K over 12 h, soaked for 40 h, heated to 1223 K over 10 h, maintained for 10 h, and subsequently cooled to ambient temperature in the finances. The obtained ingots were crushed into powders by hand milling and then densified using a spark plasma sintering (SPS) method (SPS-3T-3-MIN(T)) at 873 K for 5 min in a 10.0 mm diameter graphite die under 0.5 t pressure in vacuum. The obtained pellets were then used for measurement of thermal properties.

3 Results and discussion

Through brief high-temperature vacuum-sealed tube melting, we obtained SnS crystalized in the orthorhombic phase with the space group *Pnma*, as shown in Fig. 1b. Specifically, Sn^{2+} has three stronger Sn–S bonds and four weaker Sn–S bonds, forming a distorted SnS_7 polyhedral coordination[18,30]. Due to the lone pair electrons of Sn^{2+}, its distorted structure results in its intrinsic anharmonicity. Fig. 2a shows the powder X-ray diffraction (XRD) patterns of $Sn_{1-2x}Ag_xBi_xS$ (x=0, 0.01, 0.02, 0.03). All the main diffraction peaks match well with the standard card of SnS (PDF#14-0620) without obvious impurity peaks. The doped Ag and Bi are well distributed in the SnS matrix (Fig. 2b), and the element ratios measured by ICP–AES are close to the theoretical ratios (Table S1). Fig. 2c and Fig. 2d show the smooth surface of the pellets and the intrinsic layered structure of the doped SnS. Most previous studies doped SnS with 2% Ag[18,25], but we enhanced the dop-

DOI: 10.52396/JUSTC-2024-0025
JUSTC, **2024**, 54(6): 0601

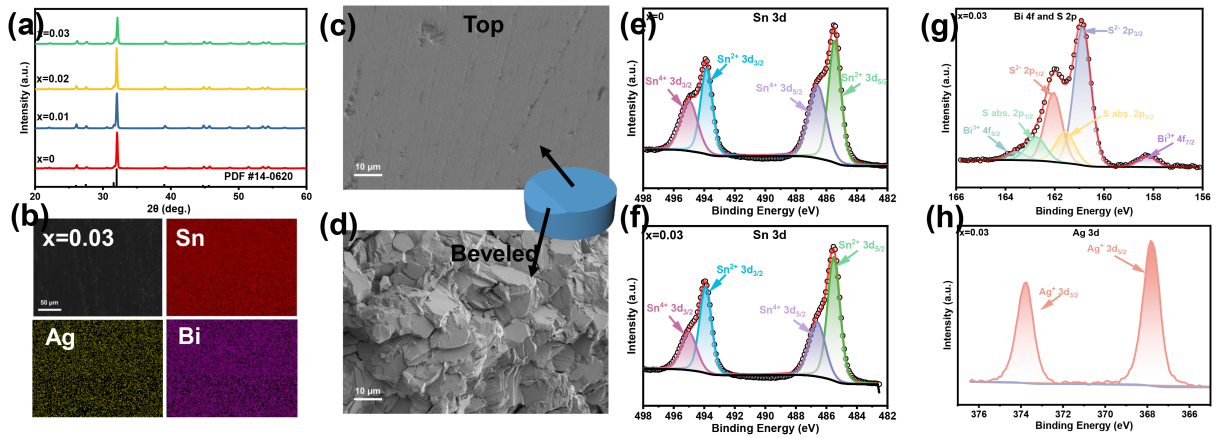

Fig. 2. (a) XRD patterns of $Sn_{1-2x}Ag_xBi_xS$ (x = 0, 0.01, 0.02, 0.03). (b) SEM–EDS mapping of $Sn_{0.94}Ag_{0.03}Bi_{0.03}S$, showing even dispersion. (c, d) SEM images of $Sn_{0.94}Ag_{0.03}Bi_{0.03}S$ pellets from top view and beveled view, respectively. XPS spectra of SnS and $Sn_{0.94}Ag_{0.03}Bi_{0.03}S$: (e, f) 3d orbitals of Sn element; (g) 2p orbitals of S element and 4f orbitals of Bi; (h) 3d orbitals of Ag element.

ing limit to 3% simply by codoping Bi with Ag. As Fig. S1 shows, when the doping amount x exceeds 0.03, a diffraction peak appears at approximately 45° attributed to the (220) plane of $AgBiS_2$ in the XRD pattern. Thus, we considered 3% to be the doping limit of Ag and Bi in SnS. When $x > 0.03$, the second phase of $AgBiS_2$ appears, demonstrating that the Ag and Bi atoms are no longer dissolved in the SnS matrix. Therefore, we believe that 3% is the doping limit of Ag and Bi in SnS.

The radii of Ag^+ and Bi^{3+} are both similar to that of Sn^{2+} in SnS, so they are less likely to induce strain field fluctuations[18,31]. Fig. S2 shows the lattice parameters deduced from XRD (PDF#14-0620, a = 11.19 Å± 0.02 Å, b = 3.98 Å± 0.02 Å, c = 4.33 Å± 0.02 Å). On the other hand, charge neutrality contributes to the improved doping limit. Fig. 2e–h shows the X-ray photoelectron spectra (XPS) of different elements in $Sn_{1-2x}Ag_xBi_xS$ (x=0, 0.03). In Fig. 2e and f, the peaks at 485.5 eV and 493.9 eV are in line with those of Sn^{2+} $3d_{5/2}$ and Sn^{2+} $3d_{3/2}$, while the peaks at 486.6 eV and 495.0 eV are assigned to the Sn^{4+} $3d_{5/2}$ and Sn^{4+} $3d_{3/2}$ orbitals, respectively. All the peaks of SnS and doped SnS are consistent, indicating that there is no variation in Sn after doping. The presence of Sn^{4+} is due to surface oxidation. As the binding energies of the S 2p orbitals and Bi 4f orbitals are in the same energy range, we plot them in the same graph (Fig. 2g). The binding energies of 160.9 eV and 162.1 eV are consistent with that of S^{2-}, while the binding energies of 161.8 eV and 163.0 eV are consistent with that of absorbed S, with a splitting energy of 1.2 eV. The peaks at 163.4 eV and 158.1 eV are assigned to Bi $4f_{5/2}$ and $4f_{7/2}$ of the trivalent Bi^{3+} ion, indicating that Bi exists in the form of Bi^{3+}. In Fig. 2h, the two peaks at 373.8 eV and 367.8 eV are attributed to Ag $3d_{3/2}$ and $3d_{5/2}$ of Ag^+, respectively. XPS confirmed that Ag and Bi were doped in the SnS matrix in the form of Ag^+ and Bi^{3+}, respectively. Monovalent Ag^+ will destroy the charge balance when replacing divalent Sn^{2+} in SnS, so its doping limit is low[25]. After adding Bi, trivalent Bi^{3+} can offset the charge imbalance, thus improving the doping limit of Ag^+. However, the doping limit can only increase to 3% (as determined by XRD), although the amounts of Ag^+ and Bi^{3+} that are equally substituted for Sn^{2+} are charge balanced. This is because Ag^+ and Bi^{3+} are inclined to accumulate to form Ag^+-Bi^{3+} pairs to maintain charge balance around the substation sites[5]. With increasing doping amount, the Ag^+-Bi^{3+} pair areas increase, and a second phase of $AgBiS_2$ appears. To conclude, we increase the doping limit of Ag in SnS from 2% to 3% by codoping with an equal amount of Bi.

We performed thermogravimetric analysis (TGA) on all the samples to test their thermal stability. As shown in Fig. S3, all the doped and undoped samples are thermally stable at temperatures up to 625 °C, and they begin to decompose at higher temperatures, consistent with previous research[21]. Thus, the samples can maintain thermal stability during preparation and measurement.

The thermal conductivity is calculated by the formula $\kappa = D \cdot Cp \cdot \rho$, where κ is the thermal conductivity, D is the thermal diffusivity, Cp is the specific heat and ρ is the density. As we can see from Fig. 3a, the thermal conductivity of $Sn_{1-2x}Ag_xBi_xS$ parallel to the press decreases significantly as x increases, from 1.367 $W \cdot m^{-1} \cdot K^{-1}$ for x=0 to 0.535 $W \cdot m^{-1} \cdot K^{-1}$ for x=0.03 at room temperature, which is lower than that in previous studies[18,21,22,29,32] (Fig. 3d). At 275 °C, the change has the same trend, but the gap decreases, and the thermal conductivity of $Sn_{0.94}Ag_{0.03}Bi_{0.03}S$ reaches 0.388 $W \cdot m^{-1} \cdot K^{-1}$, which is below the amorphous limit of SnS (0.450 $W \cdot m^{-1} \cdot K^{-1}$). Interestingly, the thermal conductivity perpendicular to the press decreases less than that in the parallel direction (Fig. 3b). This is due to the layered structure of SnS (Fig. 2c and d)[21]. Due to the 2D nature of the SnS structure, the nanosheets tile along the planes spontaneously when pressed. Thus, the thermal conductivity parallel to the sintering pressure direction is the out-of-plane thermal conductivity, and that perpendicular to the sintering pressure direction is the in-plane thermal conductivity. The former is lower than the latter[9]. As boundaries have more influence on the out-of-plane thermal conductance than on the in-plane conductance[3], the thermal conductivity parallel to the press decreases more, and the anisotropy increases.

Here, we mainly discuss the thermal conductivity parallel to the press. The thermal diffusivity has a similar trend to that

DOI: 10.52396/JUSTC-2024-0025
JUSTC, **2024**, 54(6): 0601

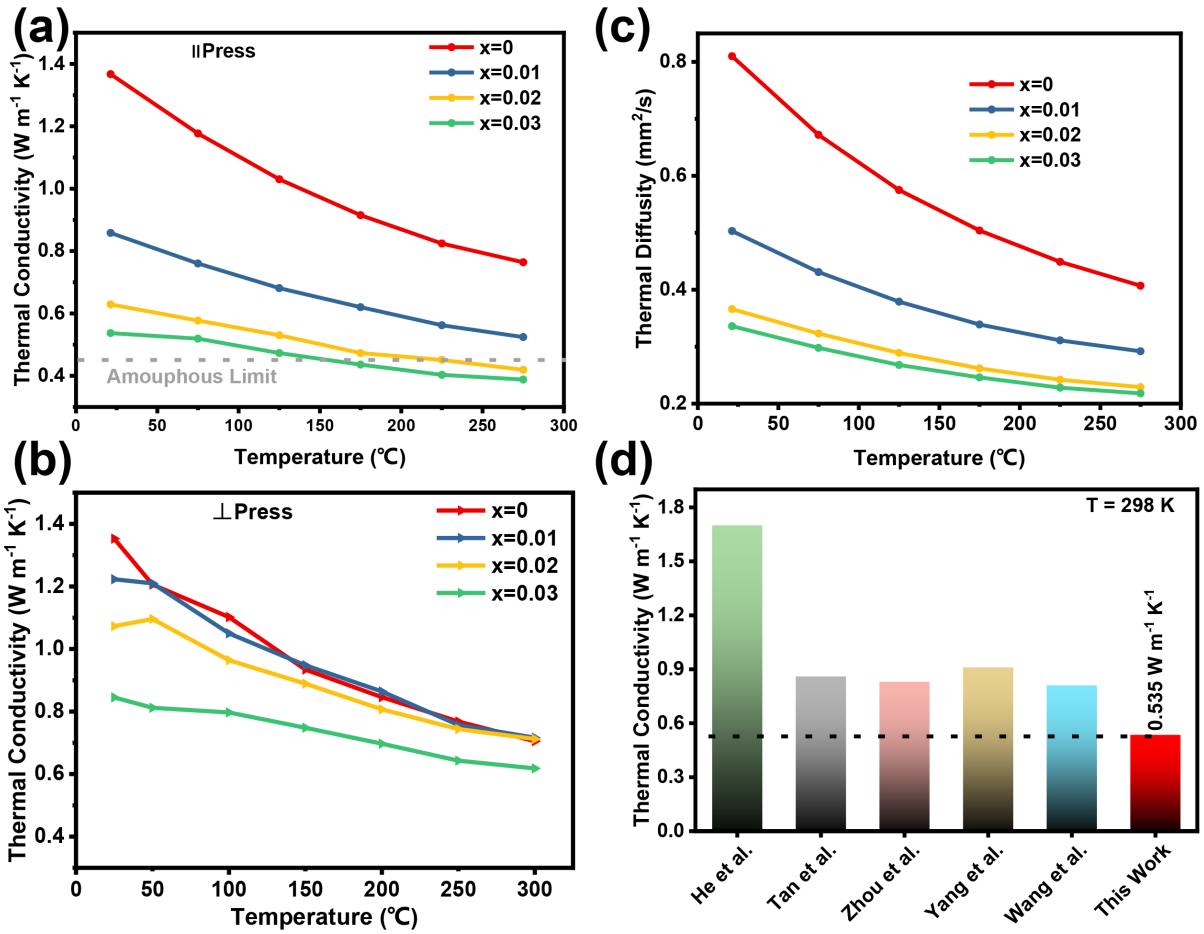

Fig. 3. Thermal transport properties of $Sn_{1-2x}Ag_xBi_xS$ (x = 0, 0.01, 0.02, 0.03). (a) Thermal conductivity parallel to the press. (b) Thermal conductivity vertical to the press. (c) Thermal diffusivity parallel to the press. (d) Compare of ultralow thermal conductivity of SnS in previous researched and this work.

of the thermal conductivity (Fig. 3c). The specific heat remains almost constant regardless of whether the variable is temperature or impurity (Fig. S4), so the variation in thermal conductivity mainly comes from fluctuations in thermal diffusivity. The thermal diffusivity can be described as $D = v^2\tau/3$, where v is the phonon group velocity and τ is the relaxation time of the phonons[6]. Furthermore, τ can be written as:

$$\tau^{-1} = \tau_D^{-1} + \tau_A^{-1} + \tau_B^{-1} = A\omega^4 + B\omega^2 T + \frac{v}{L},$$

where τ_D, τ_A and τ_B are the relaxation times contributed by point defects, anharmonic (Umklapp) phonon scattering, and boundary scattering, respectively, ω is the phonon frequency, T is the temperature, L is the grain size, and A and B are coefficients related to Rayleigh and anharmonic scattering, respectively[17]. Only τ_A is temperature dependent and proportional to T. SnS is intrinsically anharmonic, so τ_A is the dominant part of the relaxation time in pure SnS. Moreover, impurity defect scattering is suppressed in SnS, and the grains are relatively large (in contrast to doped SnS, discussed below), so the thermal conductivity (or thermal diffusivity) is proportional to τ_A, namely, T^{-1} (in Fig. S5). After Ag and Bi are doped, defects are introduced; thus, τ_D cannot be ignored. Moreover, the grain size of the ingots decreases, and the number of boundaries increases, further decreasing τ. Consequently, the κ–T (D–T) plots become flat. The influence of point defects and boundaries on the thermal conductivity will be discussed further.

Point defects (atomic scale). Doping is a conventional strategy for suppressing the thermal conductivity of solids[14,33–36]. External atoms with distinct masses and radii introduce mass fluctuations and strain. The relaxation time contributed by point defects τ_D can be expressed as[15,37]:

$$\tau_D^{-1} = \frac{\omega^4 \overline{V}}{4\pi v^3}(1-x)x\left\{[(M-M_i)/M]^2 + \varepsilon[(d-d_i)/d]^2\right\},$$

where x is the impurity concentration, M and M_i are the masses of the host atoms and dopants, respectively, ε is an adjustable strain-related parameter, and d and d_i are the radii of the host atoms and dopants, respectively. Fig. 4a shows a typical high-angle annular dark-field scanning transmission electron microscopy (HAADF-STEM) image of $Sn_{0.94}Ag_{0.03}Bi_{0.03}S$[20,38], confirming that Bi is doped into the lattice. Ag and Sn have similar atomic masses, so it is difficult to distinguish them in HAADF-STEM images. Furthermore, the doped atoms are evenly distributed in the SnS matrix at the nanoscale (Fig. 4b). Since the mass and radius of Ag^+ are not much different from those of Sn^{2+}, the thermal conductivity of Ag-doped SnS can only be as low as

DOI: 10.52396/JUSTC-2024-0025
JUSTC, **2024**, 54(6): 0601

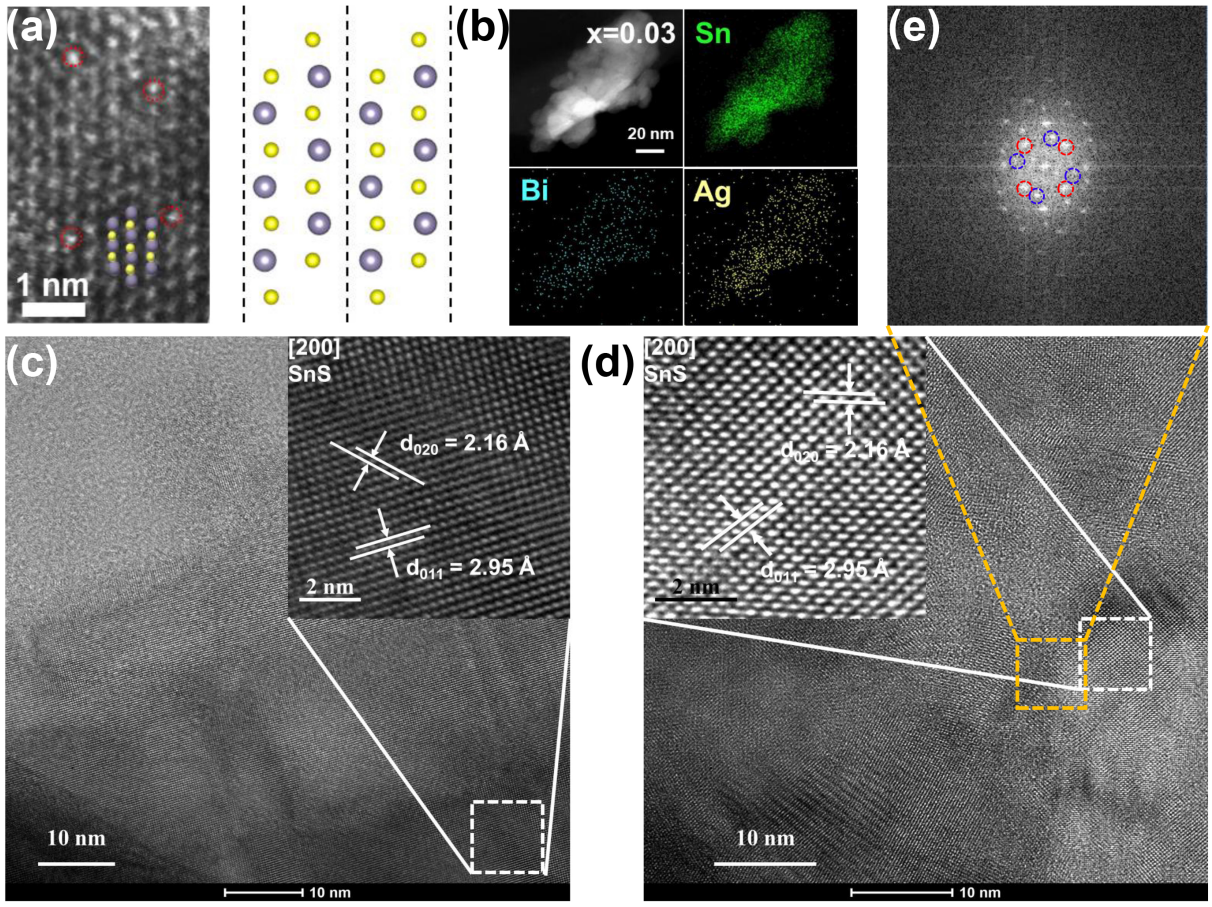

Fig. 4. (a) HAADF-STEM image of $Sn_{0.94}Ag_{0.03}Bi_{0.03}S$ along the (100) direction, where Sn and S atoms are depicted in gray and yellow; the red circles are highlighted Bi atoms. The right panel shows the crystal structure of SnS in the same projection. (b) HRTEM-EDS mapping of $Sn_{0.94}Ag_{0.03}Bi_{0.03}S$. (c, d) HRTEM images of SnS and $Sn_{0.94}Ag_{0.03}Bi_{0.03}S$, respectively. Insets are enlarged images of selected areas. (e) FFT image of the selected area in (d), showing distinct two sets of diffraction spots.

0.85–0.90 $W \cdot m^{-1} \cdot K^{-1}$ at room temperature when $x \leq 0.02$[18]. The addition of Bi, however, increased the doping amount of Ag to 3% and at the same time increased the doping amount of Bi by 3%, which increased the number of point defects by three times. It is apparent that $(1-x)x$ increased with x when $x \leq 0.5$. Moreover, the relative atomic masses of Ag, Bi and Sn are 107.87, 208.98 and 118.71, respectively. The mass gap between Bi and Sn is significantly larger, thus inducing greater mass fluctuations. For comparison, we used Cr(III) (relative atomic mass: 52.00) codoped with Ag. As Fig. S6 shows, $Ag_{0.03}Bi_{0.03}Sn_{0.94}S$ and $Ag_{0.03}Cr_{0.03}Sn_{0.94}S$ both have lower thermal conductivities than SnS. However, as the temperature increased, the thermal conductivity of $Ag_{0.03}Bi_{0.03}Sn_{0.94}S$ decreased much more than that of $Ag_{0.03}Cr_{0.03}Sn_{0.94}S$. This may be because Cr has a much lower atomic mass, so the scattering of phonons is not as strong as that of Bi. Bi is the heaviest nonradioactive element, so we believe Bi is the best codopant for Ag in SnS. Therefore, the thermal conductivity of $Sn_{0.94}Ag_{0.03}Bi_{0.03}S$ decreased to 0.535 $W \cdot m^{-1} \cdot K^{-1}$ at room temperature and decreased to 0.388 $W \cdot m^{-1} \cdot K^{-1}$ at 275 °C. For the strain field, the radius differences between Ag^{+}/Bi^{3+} and Sn^{2+} are both much less, so they can be neglected.

Boundary scattering (nanoscale). In Fig. 4c and d, we can see that SnS and $Sn_{0.94}Ag_{0.03}Bi_{0.03}S$ both have typical SnS orthorhombic lattices. However, after adding dopants, the number of boundaries increases. Fig. 4e shows the FFT images of the yellow dotted line region, and there are two distinct sets of diffraction spots for Sn, indicating that there are grain boundaries in the region. The number of grain boundaries increases upon doping with Ag and Bi, which is another reason for the decrease in the thermal conductivity of $Sn_{1-2x}Ag_xBi_xS$[39,40]. A greater number of boundaries means smaller grains, thus decreasing τ_B and the thermal diffusivity. Various abundant boundaries strongly scatter phonons with mean free paths (MFPs) at the nanoscale, thus inhibiting heat transport and further reducing the thermal conductivity.

Overall, all samples in our research are polycrystalline with grain boundaries. However, after adding Ag and Bi, the grain size shrinks, thus leading to more boundaries. Structures at different scales scatter different phonons, reduce τ_A and τ_B, and synergistically decrease the thermal conductivity to 0.535 $W \cdot m^{-1} \cdot K^{-1}$ at room temperature and 0.388 $W \cdot m^{-1} \cdot K^{-1}$ at 275 °C in $Sn_{0.94}Ag_{0.03}Bi_{0.03}S$.

4 Conclusions

Through a simple high-temperature sealing reaction, we obtained Ag/Bi codoped SnS, increasing the solubility limit of Ag in SnS from 2% to 3%, which can be determined from the XRD and EDS images. Charge-balanced codoping by substi-

DOI: 10.52396/JUSTC-2024-0025
JUSTC, **2024**, 54(6): 0601

tuting Sn^{2+} with an equal amount of Ag^{+} and heavy Bi^{3+} is an excellent strategy for realizing ultralow thermal conductivity in SnS. In the SnS matrix, the codoping of Bi increases the number of point defects, and due to the greater mass difference between Bi and Sn than between Ag and Sn, the phonon group velocity decreases more significantly. In addition, the addition of Ag and Bi also reduces the grain size of polycrystalline SnS and increases boundary scattering, and the joint effects of the two reduce the thermal conductivity of SnS to 0.535 $W \cdot m^{-1} \cdot K^{-1}$ at room temperature and 0.388 $W \cdot m^{-1} \cdot K^{-1}$ at 275 °C, lower than the amorphous limit of SnS. This work provides an effective charge balance strategy for exceeding the doping limit and achieving ultralow thermal conductivity in solids.

Supporting information

The supporting information for this article can be found online at https://doi.org/10.52396/JUSTC-2024-0025. The supporting information includes detailed characterization, XRD, lattice parameter, TGA, specific heat, correlation of temperature, comparative experiments and thermal transport properties, and ICP data.

Acknowledgements

This work was financially supported by the CAS Project for Young Scientists in Basic Research (YSBR-070), the National Natural Science Foundation of China (21925110, 21890750, U2032161, 12147105), the USTC Research Funds of the Double First-Class Initiative (YD2060002004), the National Key Research and Development Program of China (2022YFA1203600, 2022YFA1203601, 2022YFA1203602), the Natural Science Foundation of China-Anhui Joint Fund (U23A20121), the Outstanding Youth Foundation of Anhui Province (2208085J14), the Anhui Provincial Key Research and Development Project (202004a050200760), the Key R&D Program of Shandong Province (2021CXGC010302), the Users with Excellence Project of Hefei Science Center CAS (2021HSC-UE004), the Fellowship of the China Postdoctoral Science Foundation (2022M710141), and the open foundation of the Key Laboratory of the Engineering Research Center of Building Energy Efficiency Control and Evaluation, Ministry of Education (AHJZNX-2023-04).

Conflict of interest

The authors declare that they have no conflict of interest.

Biographies

Long Chen is currently a master's student at the School of Chemistry and Materials Science, University of Science and Technology of China, under the supervision of Prof. Changzheng Wu and Prof. Yongchun Zhu. His research mainly focuses on 2D materials with ultralow thermal transport properties.

Yongchun Zhu is currently a Professor at the University of Science and Technology of China (USTC). She received her Ph.D. degree from USTC in 2006. Her research interests include lithium-ion/sodium-ion batteries, aqueous batteries, metal-air battery and materials with ultralow thermal conductivity.

Changzheng Wu is currently a Professor at the University of Science and Technology of China (USTC). He received his Ph.D. degree from USTC in 2007. His research interests include preparation and characterization of two-dimensional materials with excellent physical properties, oxygen reduction catalysts and fuel cells, relevant mechanism and functional application of transition metal oxide materials.

References

[1] Liu S, Dun C C, Wei J L, et al. Creation of hollow silica-fiberglass soft ceramics for thermal insulation. *Chem. Eng. J.*, **2023**, *454*: 140134.
[2] Lin X C, Li S L, Li W X, et al. Thermo-responsive self-ceramifiable robust aerogel with exceptional strengthening and thermal insulating performance at ultrahigh temperatures. *Adv. Funct. Mater.*, **2023**, *33* (27): 2214913.
[3] Kim S E, Mujid F, Rai A, et al. Extremely anisotropic van der Waals thermal conductors. *Nature*, **2021**, *597* (7878): 660–665.
[4] Sarkar D, Ghosh T, Banik A, et al. Highly converged valence bands and ultralow lattice thermal conductivity for high-performance SnTe thermoelectrics. *Angew. Chem. Int. Ed.*, **2020**, *59* (27): 11115–11122.
[5] Zhou M, Li J F, Kita T. Nanostructured AgPbmSbTem+2 system bulk materials with enhanced thermoelectric performance. *J. Am. Chem. Soc.*, **2008**, *130* (13): 4527–4532.
[6] Qian X, Zhou J W, Chen G. Phonon-engineered extreme thermal conductivity materials. *Nat. Mater.*, **2021**, *20* (9): 1188–1202.
[7] Jana M K, Biswas K. Crystalline solids with intrinsically low lattice thermal conductivity for thermoelectric energy conversion. *ACS Energy Lett.*, **2018**, *3* (6): 1315–1324.
[8] Zhu H, Zhao C C, Nan P F, et al. Intrinsically low lattice thermal conductivity in natural superlattice (Bi2)m(Bi2Te3)n thermoelectric materials. *Chem. Mater.*, **2021**, *33* (4): 1140–1148.
[9] Gibson Q D, Zhao T Q, Daniels L M, et al. Low thermal conductivity in a modular inorganic material with bonding anisotropy and mismatch. *Science*, **2021**, *373* (6558): 1017–1022.
[10] Ji R W, Lei M, Genevois C, et al. Multiple anion chemistry for ionic layer thickness tailoring in Bi2+2nO2+2nSenX2 (X = Cl, Br) van der Waals semiconductors with low thermal conductivities. *Chem. Mater.*, **2022**, *34* (10): 4751–4764.
[11] Wang C, Xu H Y, Cheng H, et al. Interfacial ion regulation on 2D layered double hydroxide nanosheets for enhanced thermal insulation. *Sci. China Chem.*, **2022**, *65* (5): 898–904.
[12] Su B, Han Z R, Jiang Y L, et al. Re-doped p-type thermoelectric SnSe polycrystals with enhanced power factor and high ZT > 2. *Adv. Funct. Mater.*, **2023**, *33* (37): 2301971.
[13] Yuan J J, Jin K P, Shi Z, et al. Enhanced thermoelectric performance of polycrystalline SnSe by doping with the heavy rare earth element Yb. *J. Alloy. Compd.*, **2022**, *907*: 164438.
[14] Feng D, Zheng F S, Wu D, et al. Investigation into the extremely low thermal conductivity in Ba heavily doped BiCuSeO. *Nano Energy*, **2016**, *27*: 167–174.
[15] Ning S, Huberman S C, Ding Z W, et al. Anomalous defect dependence of thermal conductivity in epitaxial WO3 thin films. *Adv. Mater.*, **2019**, *31* (43): 1903738.
[16] Zhang T D, Pan W F, Ning S T, et al. Vacancy manipulation induced optimal carrier concentration, band convergence and low lattice thermal conductivity in nano-crystalline SnTe yielding superior thermoelectric performance. *Adv. Funct. Mater.*, **2023**, *33* (10): 2213761.
[17] Xie H Y, Su X L, Hao S Q, et al. Large thermal conductivity drops in the diamondoid lattice of CuFeS2 by discordant atom doping. *J. Am. Chem. Soc.*, **2019**, *141* (47): 18900–18909.
[18] Tan Q, Zhao L D, Li J F, et al. Thermoelectrics with earth abundant

DOI: 10.52396/JUSTC-2024-0025
JUSTC, **2024**, 54(6): 0601

elements: low thermal conductivity and high thermopower in doped SnS. *J. Mater. Chem. A*, **2014**, *2* (41): 17302–17306.
[19] Collin M S, Venkatraman S K, Vijayakumar N, et al. Bioaccumulation of lead (Pb) and its effects on human: A review. *J. Hazard. Mater. Adv.*, **2022**, *7*: 100094.
[20] Wu H, Lu X, Wang G Y, et al. Sodium-doped tin sulfide single crystal: a nontoxic earth-abundant material with high thermoelectric performance. *Adv. Energy Mater.*, **2018**, *8* (20): 1800087.
[21] Wang Z Y, Wang D Y, Qiu Y T, et al. Realizing high thermoelectric performance of polycrystalline SnS through optimizing carrier concentration and modifying band structure. *J. Alloy. Compd.*, **2019**, *789*: 485–492.
[22] Zhou B Q, Li S, Li W, et al. Thermoelectric properties of SnS with Na-doping. *ACS Appl. Mater. Interfaces*, **2017**, *9* (39): 34033–34041.
[23] HU X G, HE W K, WANG D Y, et al. Thermoelectric transport properties of n-type tin sulfide. *Scripta Mater.*, **2019**, *170*: 99–105.
[24] Čermák P, Hejtmánek J, Plecháček T, et al. Thermoelectric properties and stability of Tl-doped SnS. *J. Alloy. Compd.*, **2019**, *811*: 151902.
[25] Asfandiyar, Cai B W, Zhao L D, et al. High thermoelectric figure of merit ZT > 1 in SnS polycrystals. *J. Materiomics*, **2020**, *6* (1): 77–85.
[26] Cahill D G, Watson S K, Pohl R O. Lower limit to the thermal conductivity of disordered crystals. *Phys. Rev. B*, **1992**, *46* (10): 6131–6140.
[27] Guo R Q, Wang X J, Kuang Y D, et al. First-principles study of anisotropic thermoelectric transport properties of IV-VI semiconductor compounds SnSe and SnS. *Phys. Rev. B*, **2015**, *92* (11): 115202.
[28] Ding G Q, Gao G Y, Yao K L. High-efficient thermoelectric materials: The case of orthorhombic IV-VI compounds. *Sci. Rep.*, **2015**, *5*: 9567.
[29] Yang H Q, Wang X Y, Wu H, et al. Sn vacancy engineering for enhancing the thermoelectric performance of two-dimensional SnS. *J Mater. Chem. C*, **2019**, *7* (11): 3351–3359.
[30] Zhao L D, Lo S H, Zhang Y S, et al. Ultralow thermal conductivity and high thermoelectric figure of merit in SnSe crystals. *Nature*, **2014**, *508* (7496): 373–377.
[31] Chen Q L, Lu P X, Hao Y L, et al. Morphology, structure and properties of Bi2S3 nanocrystals: role of mixed valence effects of cobalt. *J. Mater. Sci. :Mater. Electron.*, **2021**, *32* (19): 24459–24483.
[32] He W K, Wang D Y, Wu H J, et al. High thermoelectric performance in low-cost $SnS_{0.91}Se_{0.09}$ crystals. *Science*, **2019**, *365* (6460): 1418–1424.
[33] Xie H Y, Li Z, Liu Y K, et al. Silver Atom Off-centering in diamondoid solid solutions causes crystallographic distortion and suppresses lattice thermal conductivity. *J. Am. Chem. Soc.*, **2023**, *145* (5): 3211–3220.
[34] Chandra S, Bhat U, Dutta P, et al. Modular nanostructures facilitate low thermal conductivity and ultra-high thermoelectric performance in n-type SnSe. *Adv. Mater.*, **2022**, *34* (40): 2203725.
[35] He J G, Xia Y, Naghavi S S, et al. Designing chemical analogs to PbTe with intrinsic high band degeneracy and low lattice thermal conductivity. *Nat. Commun.*, **2019**, *10*: 719.
[36] Xiao Y, Wu H J, Cui J, et al. Realizing high performance n-type PbTe by synergistically optimizing effective mass and carrier mobility and suppressing bipolar thermal conductivity. *Energy Environ. Sci.*, **2018**, *11* (9): 2486–2495.
[37] Xing T, Zhu C X, Song Q F, et al. Ultralow lattice thermal conductivity and superhigh thermoelectric figure-of-merit in (Mg, Bi) Co-doped GeTe. *Adv. Mater.*, **2021**, *33* (17): 2008773.
[38] Chen H L, Chen J X, Si J C, et al. Ultrathin tin monosulfide nanosheets with the exposed (001) plane for efficient electrocatalytic conversion of CO2 into formate. *Chem. Sci.*, **2020**, *11* (15): 3952–3958.
[39] Biswas K, He J Q, Blum I D, et al. High-performance bulk thermoelectrics with all-scale hierarchical architectures. *Nature*, **2012**, *489* (7416): 414–418.
[40] Tan G J, Zhao L D, Kanatzidis M G. Rationally designing high-performance bulk thermoelectric materials. *Chem. Rev.*, **2016**, *116* (19): 12123–12149.

DOI: 10.52396/JUSTC-2024-0025
JUSTC, **2024**, 54(6): 0601